INT. J. REMOTE SENSING, 1995, VOL. 16, NO. 13, 2403–2422

Principles of swell measurement by SAR with application to ERS-1 observations off the Mauritanian coast

P. FORGET, P. BROCHE

Laboratoire de Sondages Electromagnétiques de l'Environnement Terrestre, CNRS/Université de Toulon et du Var, BP132, 83957 La Garde Cedex, France

and F. CUQ

Géosystèmes, CNRS/Université de Bretagne Occidentale, Avenue Le Gorgeu, 29283 Brest Cedex, France

(Received 17 November 1994; in final form 20 February 1995)

Abstract. This paper addresses the imaging of swell waves by Synthetic Aperture Radar (SAR). We give the principles for the determination of swell parameters from image data. Wave height determination is based on a simple method derived from the quasi-linear version of the wave imaging model of Hasselmann and Hasselmann. The influence of wind waves on wave height determination is discussed. Results on coastal swell events observed by ERS-1 off the Banc d'Arguin (Mauritania) are presented. These results are compared, generally favourably, with estimates from the wave prediction model of Météo-france and from a model of swell propagation in finite depth water. However, in intermediate to shallow water, SAR wave length estimates were found to be greater than the theoretical values obtained without currents. The results are discussed in terms of swell-current interaction phenomena. A general conclusion of the study is that satellite SAR can be considered as a quasi-operational instrument for swell monitoring at low to moderate wind speeds. Also, we point out that SAR imagery can henceforth be envisaged for physical studies on swell propagation in the coastal zone.

1. Introduction

Satellite Synthetic Aperture Radar (SAR) is now recognized to be, at least potentially, a powerful tool for monitoring ocean waves, with possible applications in wave forecasting, wave statistics and wave modelling in the coastal ocean. Much attention and effort have been paid these last 15 years to the understanding and modelling of the different mechanisms involved in the SAR wave imaging process (Alpers *et al.* 1981, Hasselmann *et al.* 1985, Kasilingam and Shemdin 1990). Data from Seasat (Macklin and Cordey 1991), SIR-B (Monaldo *et al.* 1993) and ERS-1 (Tilley and Beal 1994) satellite missions, and airborne experiments (Rufenach *et al.* 1991) have been extensively used to assess the SAR technique for remote sensing ocean waves with the goal, which is important for operational perspectives, of measuring the two-dimensional wave spectrum (it should be noted that this information is not accessible quantitatively from visible imagery). It is only recently, owing to a significant improvement in the ocean wave spectrum SAR imaging theory (Hasselmann and Hasselmann 1991), that reliable inversion techniques have been envisaged for extracting the directional wave spectrum from SAR data. Uncertainties, however, still remain concerning terms of the SAR wave modulation transfer

0143–1161/95 $10.00

function, particularly the hydrodynamic term which is a current subject of research. On the other hand, the non-linearities of the imaging process results in an azimuthal fall-off of SAR wave spectra (e.g. Beal *et al.* 1991), which restricts the detection to the short azimuthal wave components of the wave spectrum which, therefore, can be only partially reconstructed.

We start from the present state of the art of SAR remote sensing of ocean waves to envisage swell monitoring by SAR. Swell designates narrow-bands, long-crested components of a low wave number of the sea state, which occur frequently in the ocean, like the Atlantic in the case of the present study. Swell observations and predictions are demanded in a number of human activities such as off-shore oil operations, coastal management, navigation (see, for example, Mettlach *et al.* 1994). Also, short and long term series of swell measurements are needed at prescribed sensible coastal regions for which swell constitutes the main dynamical process (beach erosion, littoral currents and subsequent sediment transport, see, e.g. Carter 1988).

We will present the principles of swell measurements by SAR in §2, swell observations from ERS-1 SAR images of a coastal zone off Mauritania in §3, and comparisons of the results with wave modelling in §4. This work aims to demonstrate that swell monitoring by SAR is already feasible and that spaceborne SAR systems, like on ERS-1 satellite, allow the observations and measurements to be made at suitable spatial scales (the image size being of, typically, $100 \times 100\,\mathrm{km}^2$) for studying the spatial variations experienced by swell in the coastal zone, due to its interactions with bathymetry and currents.

2. Principles of swell measurements by SAR

The purpose of the study is to obtain maps of the main swell characteristics from SAR imagery. The mapping process consists in deriving, from the images, the spatial distributions of the swell wave number **K** and significant height H, and to represent them on a documented (coast lines, depths) regional chart. Other products than **K** could also be envisaged, like wave orthogonals or wave rays. The swell parameters are computed from the spectral analysis of small imagettes segmentating the original images, of more than 8000×8000 pixels for the case of ERS-1 Precision Product Images -PRI- (nominal spacing $\Delta = 12{\cdot}5\,\mathrm{m}$). The size of the imagettes must be chosen in order to sample the swell systems at spatial scales typical of their variability. For the images studied in §3 and §4, a constant size of $6{\cdot}4 \times 6{\cdot}4\,\mathrm{km}^2$ (512×512 pixels at nominal spacing) appeared suitable in most cases. The assumption is made that the wave field pattern is homogeneous over an imagette of this size, which is not always satisfied: indeed, wave patterns can change significantly over short distances at some places of, for instance, rapidly changing bathymetry, as in figure 1. Similar observations of dramatic changes of the wave field by bottom topography have already been reported on high-resolution visible images (Cuq 1992). It should be noted that an irregular grid, adapted to the properties of homogeneity of the signal, could be designed for image segmentation.

2.1. *Derivation of the wave modulation spectrum*

In general, SAR images and spectra are contaminated by speckle and micro-correlation effects. Speckle originates in essence from interference of the signals backscattered by the radar cell elements. Image speckling is well described by the multiplicative white noise model, which has been extensively used in statistical

studies of SAR image noise (see, recently, April and Harvey 1991, for Seasat imagery, and Olivier and Vidal Madjar 1994, for ERS-1 imagery). Correlations between neighbouring pixels are produced during the formation of the radar image and by operations of resampling. In satellite images, they are generally small for space lags greater than the resolution (Lee 1981, Forget 1994). As a check, table 1 gives the mean correlation coefficients obtained for ERS-1 PRI images. The values were obtained from featureless homogeneous imagettes of the data set used in the present study. In continuous notation, the correlation coefficient function, $c(\mathbf{r})$, is defined by:

$$c(\mathbf{r}) = \frac{<(z(\mathbf{x})-\bar{z})(z(\mathbf{x}+\mathbf{r})-\bar{z})>}{\sigma_z^2} \tag{1}$$

where $z(\mathbf{x})$ designates the pixel intensity at position $\mathbf{x}$ of the imagette, of mean $\bar{z}$ and variance $\sigma^2{}_z$ over the imagette, and $<.>$ is the operator of statistical mean. Values of $c(\mathbf{r})$ are found negligible for a lag r greater than 3Δ, small for $r=2\Delta$ and become important for $r \leqslant \Delta$ (a small asymmetry azimuth/range can be noticed). These results reflect essentially the fact that the SAR resolution, δ, of 30 m, is more than twice the pixel sampling step Δ. For the same (3-looks) imagettes, the contrast parameter of speckle intensities, $m=\sigma_z(\bar{z})^{-1}$, was estimated to 0·60 (standard deviation: SD $=0{\cdot}02$), which value is practically the same as that obtained by Olivier and Vidal Madjar (1994) for a totally different set of data (0·59). By comparison, m was of 0·28 for the 4-looks Seasat images (Lee 1981).

The imagettes being sampled at steps high enough to overcome micro-correlations between pixels, typically $\Delta_s=2\Delta$, the image intensity can be modelled by:

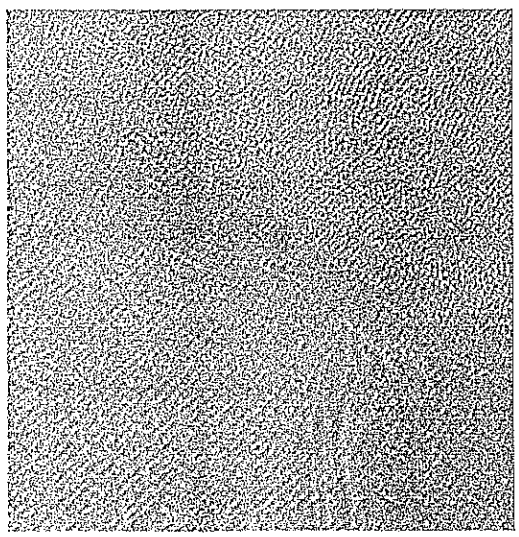

Figure 1. An imagette of 1024×1024 pixels (pixel spacing: 12·5 m) showing sharp contrasts of the swell field pattern due to bathymetry. Internal waves can be seen in the lower part of the imagette. Extracted from an ERS-1 image of the Banc d'Arguin (25 November 1992, at 23h38 UT). Coordinates of the center of the imagette are (45 km, 85 km) in the reference frame of figure 5 below.

Table 1. Mean values of the correlation coefficients for ERS-1 imagettes of noise only, as determined from an image of the Banc d'Arguin region (7 January 1993). Means have been computed from 12 featureless imagettes of 128×128 pixels, east of Cap Blanc. One pixel lag corresponds to the nominal pixel spacing (12·5 m).

	In range				
Pixel lag	−2	−1	0	+1	+2
In azimuth					
−2	0·025	0·046	0·061	0·043	0·024
−1	0·102	0·332	0·495	0·329	0·100
0	0·185	0·662	1·000	0·662	0·185
+1	0·100	0·329	0·495	0·332	0·102
+2	0·024	0·043	0·061	0·046	0·025

$$z(\mathbf{x}) = s(\mathbf{x})w(\mathbf{x}) \tag{2}$$

where $s(\mathbf{x})$ represents a white noise process modelling the speckle and $w(\mathbf{x})$ designates the image modulation by waves (equal to unity for images of pure speckle). The wave modulation spectrum is defined by:

$$S_w(\mathbf{k}) = (2\pi)^{-2} \int\int < w(\mathbf{x})w(\mathbf{x}+\mathbf{r}) > \exp(-j\mathbf{k}.\mathbf{r}) d^2\mathbf{x} \tag{3}$$

and we find, after calculations identical to those of Goldfinger 1982 (made on 1-D signals, however), the following expression of S_w in function of the image intensity spectrum S_z.

$$S_w(\mathbf{k}) = \frac{1}{\bar{z}^2}\left(S_z(\mathbf{k}) - \frac{m^2}{1+m^2}\bar{z}^2\right) \tag{5}$$

for $\mathbf{k} \neq \mathbf{0}$. Disregarding the multiplicative term, this equation states that the spectral signature of the speckle consists of a deterministic constant term added to the spectrum of the geophysical (wave) modulations. Swell parameters will be derived from imagette spectra calculated by (5). Figure 2 is a typical wave modulation spectrum of a swell event. The spectrum has been set to zero in the vicinity of the zero frequency and smoothed.

2.2. *Determination of swell characteristics*

According to the theory of Hasselmann and Hasselmann (1991), the mapping of the ocean wave spectrum $F(\mathbf{k})$ into the SAR image spectrum $S(\mathbf{k})$ (suffix 'w' has been left out) can be written as:

$$S(\mathbf{k}) = \sum_{n=0}^{\infty} T_n(\mathbf{k})(k_x\beta)^n \tag{6}$$

where β is the radial distance-to-platform velocity ratio, k_x is the azimuthal component (along the flight axis direction) of the wave number $\mathbf{k}$ and $T_i(\mathbf{k})$ are the Fourier transforms of functions of $\mathbf{r}$, themselves calculated by inverse Fourier transform operations involving, in particular, the directional wave spectrum $F(\mathbf{k})$. S

is symmetric with respect to the origin. If we assume that the sea state consists in a single, uniform, wave component of wave number $\mathbf{k}=\mathbf{K}$, $F(\mathbf{k})$ can be modelled by a delta function and it can be shown easily from (6) that $S(\mathbf{k})$ reduces to delta lines at wave numbers $p\mathbf{K}$ where $p=0, \pm 1, \pm 2, \ldots$ A similar result is obtained by considering, instead of a purely monochromatic wave, a narrow-band wave train. Figure 3 shows an example of the SAR spectrum of a swell system with a spectrum represented by:

$$F(\mathbf{k})=F_{\max}\exp\left(-\frac{|\mathbf{k}-\mathbf{K}|^2}{2\sigma^2}\right) \tag{7}$$

The SAR spectrum was computed from an image of 128×128 pixels with a spacing of 25 m, and ERS-1 conditions were envisaged. The spectral width of the wave spectrum, σ, is of 0·00137 rd m^{-1} (corresponding to a -10 dB width of 3 spectral intervals) and the significant wave height, H, and wave length, Λ, are of 1·5 m and 150 m, respectively. The image spectral energy is concentrated around $\pm\mathbf{K}$, $\pm2\mathbf{K}$ and $\pm3\mathbf{K}$, most of it being contained in the first two (symmetric) peaks, which has been verified on a variety of realistic swells. These peaks, at $\pm\mathbf{K}$, will be regarded as the 'swell peaks' of image spectra.

These results show that a narrow-band wave system at wave number $\mathbf{K}$ is imaged into a modulation of the same wave number, whereas, for a broad-band wave spectrum (as a wind wave spectrum), the position of the wave spectral peak can be misplaced on the SAR spectrum by the imaging process (e.g. Alpers 1983, Ocampo-Torres and Robinson 1989, Rufenach *et al.* 1991). We will assume in the following that the actual sea state consists of a swell narrow-band enough to overcome any wave number distortion of the wave spectral peak on radar image spectra. The narrow-band assumption is satisfied in many real situations since wave systems

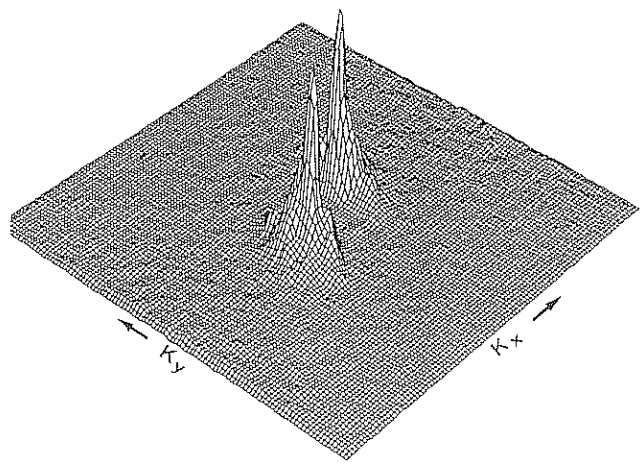

Figure 2. A typical wave modulation spectrum off the Banc d'Arguin. k_x is the azimuthal axis. The two peaks correspond to a swell of wave length 280 m and propagating southeastward. Computed from an imagette of 128×128 pixels, with a pixel spacing of 25 m, extracted from the same image as in figure 1. Coordinates of the center of the imagette are (−20 km, 205 km) in the reference frame of figure 5 below. Wave number coordinates are in the range $[-(50\,\mathrm{m})^{-1}, +(50\,\mathrm{m})^{-1}]$. The spectrum has been smoothed.

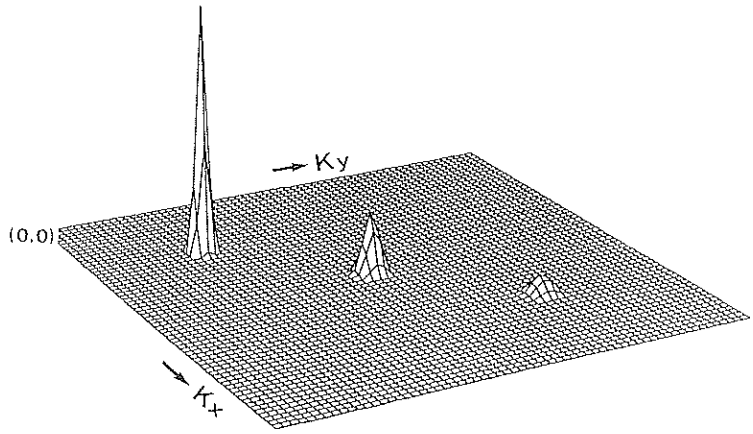

Figure 3. The theoretical SAR spectrum of a narrow-band swell propagating at 45° from the azimuthal direction. Imagette size in 128×128 pixels and pixel spacing is 25 m. Swell wave length is 150 m, significant wave height is 1·5 m and spectral width (equation (7)) is 0·00127 rd m^{-1}. Wave number coordinates are in the range [0 m^{-1}, (50 m)$^{-1}$].

emanating from a storm undergo, due to dispersion, a natural filtering with distance and far from the storm, they can present locally, a quasi-monochromatic aspect (Goda 1985). The presence of wind waves can disturb, more or less profoundly, the swell part of the wave spectrum, depending on the energy and period of the swell with respect to the wind sea spectrum characteristics (Goda 1985). The present theory envisages the cases where wind waves and swell are decoupled in the wave number spectral domain (no interactions between the two wave systems).

So, the swell wave number $\mathbf{K}$ can be theoretically identified with the estimate $\mathbf{k}_m$ of the position of one of the two (symmetric) peaks detected on the SAR wave modulation spectrum, of energy E. In practice, $\mathbf{k}_m$ and E are estimated from the first- and second-order spectral moments computed within a window around the SAR spectral peak. In § 3 and § 4, analysis will be performed with a window width of four spectral intervals with an image size of 256×256 pixels (pixel sampling $\Delta_s = 25$ m).

The swell wave spectrum can be computed by inversion of the complete model expressed by (6) (Hasselmann and Hasselmann 1991, Krogstadt *et al.* 1994). However, since a single ERS-1 image consists of up to 245 imagettes of the size chosen here, this solution appears computationally costly. By treating SAR swell peaks as delta functions, as done previously, the swell energy M is solution of (6), properly integrated around $\pm\mathbf{K}$. Rather than following this way, we investigated the method consisting of deriving M from the so-called 'quasi-linear' (QL) version of the complete model, which gives simply, after integration:

$$E = |T^s(\mathbf{K})|^2 \frac{M}{2} \exp\left(-\beta^2 K_x^2 |T^v(\mathbf{K})|^2 M\right) \tag{8}$$

T^s represents the linear SAR modulation transfer function and T^v is a geometrical term. Both terms being of constant use in the literature of SAR imaging of ocean waves, they will not be given here (see, e.g. Hasselmann and Hasselmann 1991).

In order to assess the pertinence of the QL model in conditions of swell, this model and the complete model have been compared on imagettes of 128×128 pixels

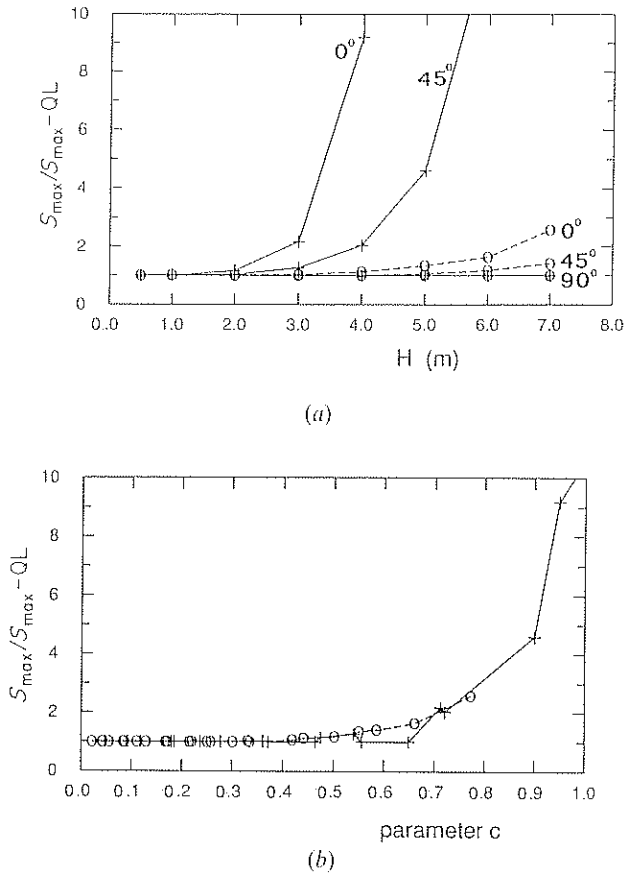

Figure 4. The ratio between the peak amplitude of the swell SAR spectrum as calculated by the complete spectral imaging model and by its quasi-linear approximation, versus significant wave height (*a*), and parameter *c* given by equation (10) (*b*), for two swell wave lengths (150 m: ——, 250 m: ----) and three directions of swell propagation (0° is for an azimuth travelling swell).

(spacing 25 m), with ERS-1 parameters and for a variety of swell characteristics: $\Lambda = 150$ m and 250 m; Φ (swell direction with respect to the azimuthal axis) varying from 0° to 360°; $H(=4\sqrt{M})$, varying from 0·5 m to 7 m. The swell spectrum was modelled by (7) with $\sigma = 0{\cdot}00274$ rd m^{-1} (corresponding to a -10dB width of six spectral intervals for actual imagettes) and $F_{max} = 1320H^2$. Figure 4(*a*) gives the ratio between the peak amplitude of the SAR spectrum, S_{max}, as given by the complete model, and the peak amplitude deduced from the QL model, S_{max}^{QL}, which can be written as:

$$S_{max}^{QL} = |T^s(\mathbf{K})|^2 \frac{F_{max}}{2} \exp\left(-\beta^2 K_x^2 |T^v(\mathbf{K})|^2 M\right) \tag{9}$$

As can be seen on the figure, QL estimates agree with the complete model estimates for swells travelling in range direction ($\Phi = 90°$ or 270°). Discrepancies are observed with decreasing Λ and as the swell direction deviates from the range direction. In any

case, the QL approximation of the complete model supports swells of steepness lower than 0·013. In figure 4(*b*), the theoretical results of figure 4(*a*) are plotted versus the non-dimensional parameter c given by:

$$c=\frac{H}{4}\beta(Kg)^{1/2}K_x(\cos^2\theta_i+\sin^2\theta_i\sin^2\Phi)^{1/2} \tag{10}$$

where θ_i is the incidence angle (23° here). c was introduced by Alpers *et al.* (1981) to define the degree of non-linearity of the velocity bunching mechanism. The diagram shows that, empirically, the QL and complete models are in agreement for, typically, $c<0{\cdot}6$. It can be noted that this value is twice the value for which the imaging by velocity bunching turns from linear to non-linear (Alpers *et al.* 1981, Alpers 1983). Also, it should be noted that our measurements of $S_{\max}/S_{\max}^{QL}$ are nicely organized, along a single curve, in figure 4(*a*). We found no theoretical argument for this.

To resume at this point, (8) offers a simple and suitable model for evaluating swell wave energy or height for a variety of conditions, with no restriction for range or near range propagating swells, restricted to swells of moderate steepness for azimuthal or near azimuthal propagating swells.

Finally, we have to discuss how the presence of wind waves can affect the method proposed for estimating the swell wave height. The major influence of wind waves for the present purpose is to contribute to the smearing of the SAR image in the azimuthal direction, resulting, in the spectral domain, in a fall-off of spectral amplitudes in azimuth. The shape of the fall-off function depends on the parameters of the wind sea state, which are not *a priori* known. This fall-off phenomenon has been studied, both theoretically and experimentally, at many times during the last decade (e.g. Beal *et al.* 1983, Lyzenga 1986, Rufenach *et al.* 1991, Johnsen *et al.* 1991). For a Pierson-Moskowitz (PM) fully-developed wave spectrum (Pierson and Moskowitz 1964), the fall-off wave length in azimuth, i.e. the wave length at which the spectral response falls to 0·61 of its maximum value, is given by (Monaldo and Lyzenga 1986):

$$\lambda_c=3{\cdot}93\beta\sqrt{H_w} \tag{11}$$

or alternatively:

$$\lambda_c=0{\cdot}57\beta W \tag{12}$$

where H_w is the significant wave height of wind waves and W is the wind velocity. With β of the order of 110 s, as for Seasat or ERS-1, λ_c is dramatically high, even at low winds. For example: $\lambda_c=314$ m for $W=5\,\mathrm{m\,s^{-1}}$. In fact, investigations of SIR-B and Seasat images have shown that λ_c was significantly lower than predicted by (11) or (12) (Monaldo and Lyzenga 1986), which could be explained partly by the fact that not all the waves contribute to the azimuthal smearing of SAR spectra, but only the waves with wave length less than twice the SAR resolution (Tucker 1985). To proceed, we expect from (12) a small influence of wind waves on SAR swell peaks amplitude if the azimuthal component of the swell wave number, $K_x=(2\pi/\Lambda)\cos\Phi$, is lower than $2\pi/\lambda_c$, implying:

$$W<\frac{\alpha\Lambda}{\cos\Phi}\equiv W_c \tag{13}$$

with $\alpha=(0{\cdot}57\beta)^{-1}=0{\cdot}016\,\mathrm{s^{-1}}$ for $\beta=110$ s. For example $W_c=5{\cdot}6\ \mathrm{m\,s^{-1}}$ for $\Lambda=250$ m, $\Phi=45°$. (13) constitutes a rather restrictive condition for swell height

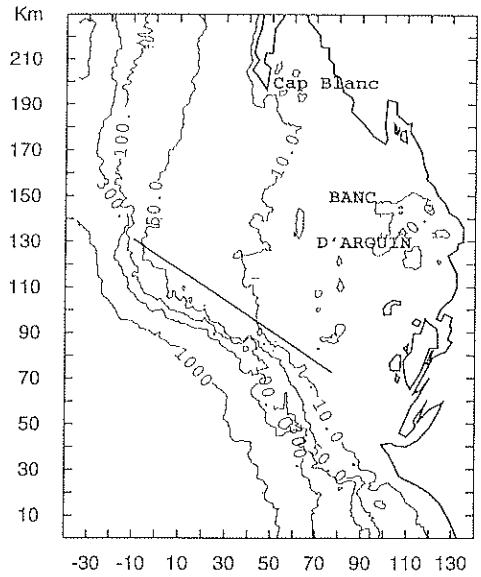

Figure 5. The region of the Banc d'Arguin (Mauritania). Coordinates of the centre of the map are (N 20°15′, W 17°00′). The transect of figure 7 below is made along the segment indicated on the map.

estimates by the present method. However, it must be kept in mind that a fully-developed sea is not common in the ocean and that, accordingly, (13) gives a lower limiting value for the wind velocity W. For example, we computed the parameter α in fetch-limited conditions, α_J, by using the JONSWAP formulae of the variations with wind and fetch of the wave spectrum parameters (Hasselmann *et al.* 1976). We found:

$$\alpha_J = 7{\cdot}2\alpha \tilde{X}^{-0{\cdot}22} \tag{14}$$

where $\tilde{X}$ is the non-dimensional fetch ($=Xg/W^2$, where X is the fetch in metres). (14) implies that the maximum wind velocity supported by our method of inversion can be substantially greater than W_c as given by (13), for instance, $6{\cdot}3\,\mathrm{m\,s^{-1}}$ for $\tilde{X}=5000$, and $8{\cdot}9\,\mathrm{m\,s^{-1}}$ for $\tilde{X}=1000$, instead of $5{\cdot}6\,\mathrm{m\,s^{-1}}$ as determined previously.

3. Swell observations by ERS-1 SAR

A set of 11 ERS-1 images off the Mauritanian coast (region of the Banc d'Arguin, figure 5), all presenting a phenomenon of swell, have been processed on the basis of the principles described above. The Banc d'Arguin region has often been investigated by the scientific community (see recently, Wolff *et al.* 1993) in the context of ecological studies and also of physical studies addressing the hydrological (upwellings, tropical front) and climatological peculiarities present. This region is located at the interface between northern and southern climatic and oceanic influences, and its ecotone functioning has a major importance, in particular, for the renewal of Mauritanian marine resources. The Banc d'Arguin itself forms a remarkable structure. It is a vast semi-circular accumulation of sediments with an average depth of 5 m, which quasi-separates the littoral domain from the ocean. It is recognized that swell is an important phenomenon contributing to the dynamics of

the Banc d'Arguin geomorphology, but only sparse observations are available, in particular due to the logistical difficulties for instrumenting the sea area concerned. ERS-1 imagery was thought to be a valuable tool for swell observations in this region. Swell is known, by fishermen and seafarers, to occur very frequently, and this has been empirically attested by the fact that swell was present on all the radar images ordered for this study independently of environmental conditions.

The dates of the scenes are listed in table 2 along with local wind measurements (meteorological station of Nouadhibou) and tidal conditions (near Cap Blanc). Examples of swell maps are presented on figure 6. H measurements are given in isolines and grey levels, and swell wave lengths and directions by the arrows. These maps illustrate attractively the geophysical products that can be brought by ERS-1 SAR in image mode. Each full ERS-1 image necessitates 1 hour of computing time on a HP9000 workstation.

Refraction is clearly observed as the swell propagates over intermediate/shallow water, e.g. at depths lower than 50 m or so, depending on the incident swell, of wave length Λ_0. For example, refraction is experienced from deeper water depths by the very long swell of figure 6(*b*) ($\Lambda_0 = 368$ m) than in figure 6(*a*) ($\Lambda_0 = 289$ m). Refraction is particularly pronounced in the region of high bathymetric gradients extending southeastward at the southern limit of the Banc d'Arguin.

Swell is not present, or it is barely detectable, in very shallow water. The eastern limit of detection corresponds roughly to the iso-depth 10 m. In fact, a detailed inspection of the images revealed that swell rarely disappears suddenly, nor is its wave number so close to the Nyquist wave number imparted by image resolution ($2\pi/60$ rd m^{-1}) that the signal-to-noise ratio drastically decreases. Rather, swell modulation amplitudes decrease gradually, as it could result in dissipation (breaking events) or bottom interaction (like bottom friction) processes (Shemdin *et al.* 1980). Figure 7 is an example of the variations of the radar modulation amplitude with water depth from 80 m to less than 5 m for a transect along which refraction was low.

We did not observe wind wave systems, but this does not mean that wind waves were not present. The wind blowing generally from the northeast sector, fetch-limited conditions are expected for the corresponding wave systems, whose peak

Table 2. Dates of ERS-1 images and environmental conditions. Nb is the number of consecutive images at our disposal for the date.

Date	Time (Ut)	Nb	Sea level (m)	Tidal phase	Wind	
					Sector	Velocity (m s^{-1})
25.11.1992	23h38	2	1·44	HT − 40′	NE	7
3.12.1992	11h41	1	0·72	LT + 10′	NE	8
30.12.1992	23h37	3	0·82	LT + 3h	N	9
7.1.1993	11h41	3	1·17	HT + 1h30′	E	11
23.1.1993	11h38	1	1·26	HT − 55′	ENE	11
26.1.1993	11h43	1	1·09	HT − 1h50′	E	7

HT = high tide; LT = low tide.

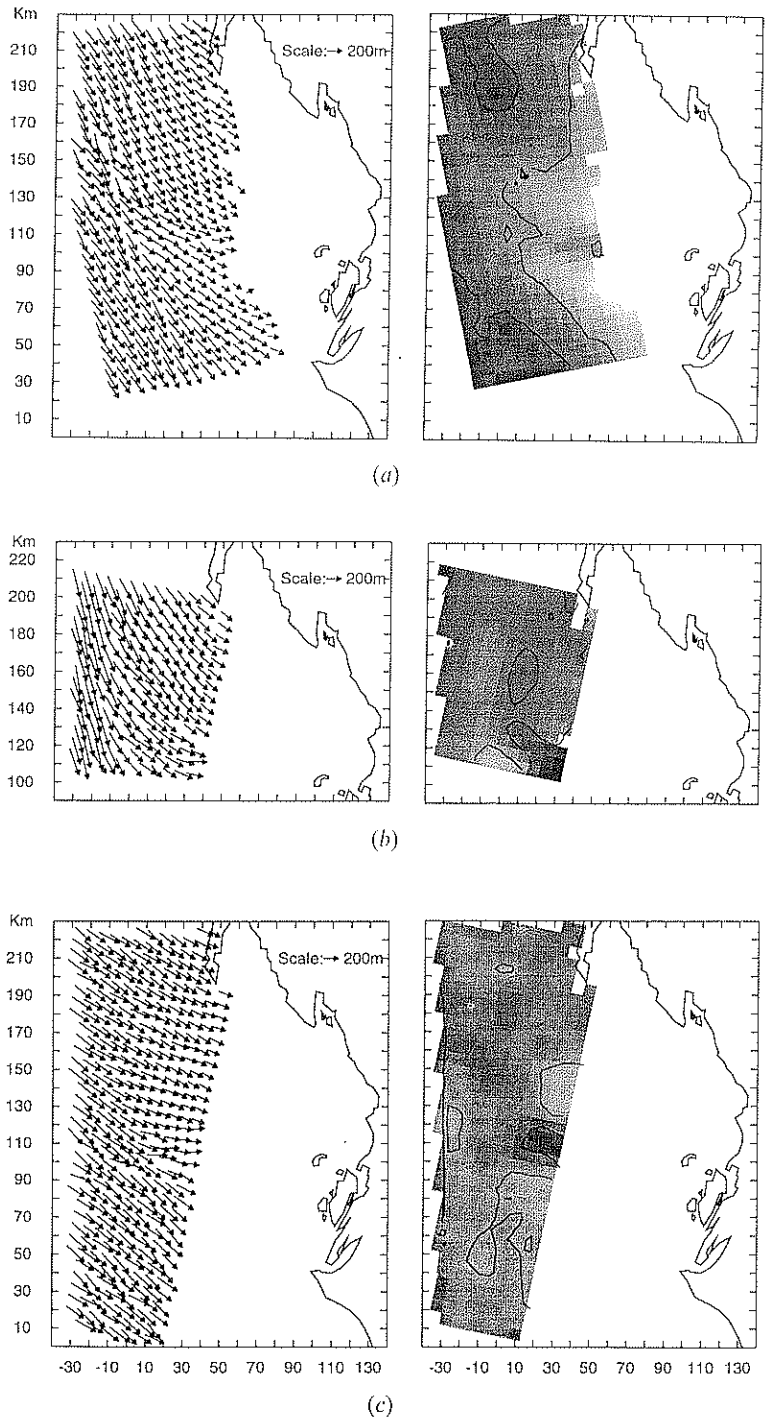

Figure 6. Example of swell maps in the region of the Banc d'Arguin. From ERS-1 images of (*a*) 25 November 1992, at 23h38, (*b*) 3 December 1992, at 11h41, (*c*) and 7 January 1993, at 11h41. Left side: maps of wave lengths and directions. Right side: maps of the significant wave height in grey scale (bright: 0·1 m, dark: 1·2 m) and iso-lines (0·4 m and 0·6 m)

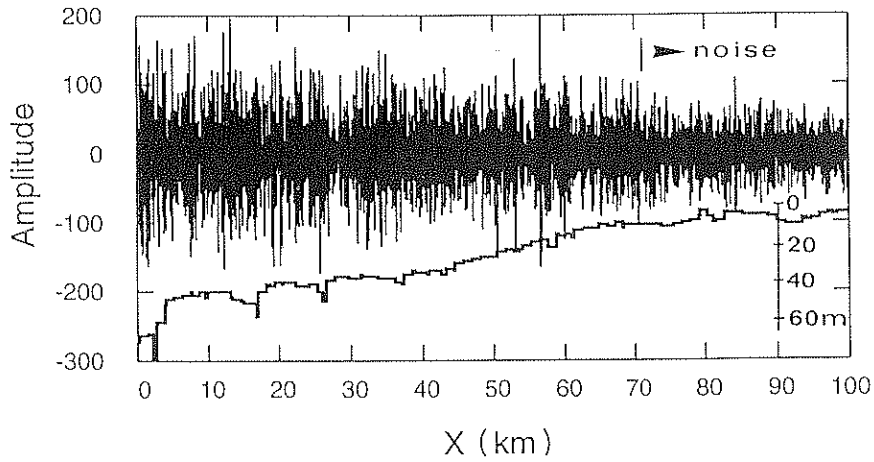

Figure 7. A transect across an ERS-1 image along which refraction is low (30 December 1992, at 23h37). This transect is geo-localized in figure 5. The signal (8000 pixels) has been band-pass filtered at 250 m ± 80 m. Water depths are given by the lower curve. To the right of the arrow, the swell signal has a poor signal-to-noise ratio, so that swell is not or hardly detected.

period T_p might not exceed, from JONSWAP formulae with $W = 10\,\mathrm{m\,s^{-1}}$ and $X = 100\,\mathrm{km}$, the value of 6·1 s, corresponding to a wave length of 57 m[1]. This value being less than twice the SAR resolution, waves of this wave length cannot be imaged. We may notice that, even if they were longer, the present geometrical conditions (in terms of the angle between the wave direction of propagation and the azimuthal direction) would not generally be favourable for their detection.

The relatively high values of the wind speed (see table 2) suggest that the actual wave height measurements may be affected by the presence of wind waves, following the discussion at the end of § 2.2. We computed the values of W_c defined in (13), representing the maximum value of the wind velocity for which the method for estimating swell wave heights is, theoretically, valid. In figure 8, W_c is plotted against the meteorological wind velocity W. For the sake of representation, since W_c can be very high for small values of $|\cos\Phi|$, only the cases corresponding to swells propagating close to the azimuthal axis ($|\cos\Phi| > 1/\sqrt{2}$) have been considered in the figure. Generally, W_c is lower than W, meaning that wind conditions are not favourable for precise wave height measurements. But it should be recalled that W_c is a very coarse parameter for qualifying our method of wave height inversion and that it represents, in fact, an underestimate of the true value under consideration. In conclusion, our SAR measurements of the significant wave height of the swell are at the limit of validity of the method proposed or, at worst, not too far from this limit.

[1] We mention at this point that, in general, the directional wave spectrum in **k** peaks at a wave number of modulus k_p which is not simply the transform $4\pi^2/gT_p^2$ of the peak frequency $1/T_p$ of the directional frequency spectrum. For example, the PM wave spectrum leads to: $k_p = \sqrt{5/8}\,4\pi^2/gT_p^2$. But this is roughly true for the JONSWAP spectrum (with a peak enhancement factor of 3·3), which explains that T_p can be directly converted into wave length λ_p by the dispersion relationship: $\lambda_p = gT^2{}_p/2\pi$.

4. Comparisons with predictions

Table 3 presents the mean swell chracteristics T_0 (period), Ψ_0 (angle of swell propagation referred to the west-east axis), Λ_0 and H_0 measured in deep water for all the radar scenes studied. Only imagettes for which Kd was greater than 10 (d is water depth) have been selected for the estimates. Period T_0 was derived from Λ_0 owing to the linear dispersion relationship of surface gravity waves. These characteristics were compared to the values T_0^{mod}, Ψ_0^{mod}, Λ_0^{mod} and H_0^{mod} computed from the wave spectra of the operational wave prediction model of Météofrance (VAGATLA). We employed the same protocol as for SAR spectra for calculating the swell characteristics Ψ_0^{mod} and Λ_0^{mod} (centroid method within a window around the spectral peak). H_0^{mod} was deduced from the peak energy estimates E_0^{mod} by: $H_0^{\text{mod}} = 4\sqrt{E_0^{\text{mod}}}$. The agreement between the two data is generally good for wave length, period (rms of differences: 1·2 s) and direction (10°·4) estimates. SAR-derived wave heights are slightly smaller than model estimates. To explain this, we examined, first, the influence of wind waves on radar estimates, as was done above for individual swell data. Values of W_c (13) and W are given in the table. It can be seen that W_c is of the order of W, except for one case (30 December 1992) where W_c is appreciably lower than W, implying that sea state conditions are reasonably well within the conditions of validity of the method for calculating H. Another reason that might be responsible for the discrepancies between SAR measurements and the values given by the wave model could lie in the expression retained for the linear SAR modulation transfer function, which is regularly put into question by specialists (see, very recently, Brüning *et al.* 1994). Finally, we should keep in mind that wave forecasts do not represent the sea truth, and that the SAR-derived wave heights could be, really, lower than the values given by the wave model.

Swell patterns in finite-depth water have been compared with the results obtained by a kinematical wave refraction model based on the classical linear ray theory. The model adopts the formulation of ray curvatures of Mathiesen (1987), and follows the numerical scheme of Griswold (1963). Due to a lack of in-situ documentation, no current was considered. The SAR-derived mean swell characteristics of table 3 were used as inputs to the model. An overall agreement was found between SAR

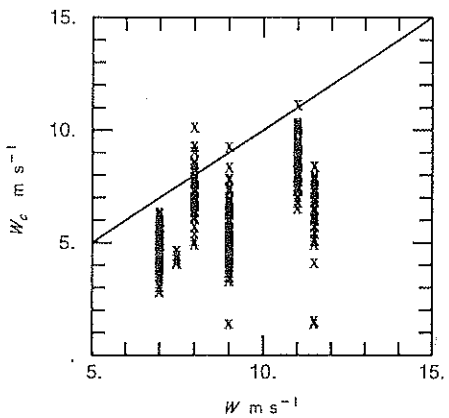

Figure 8. Wind speed parameter W_c of equation (13) versus the meteorological wind speed W measured on the shore for swells propagating close to the azimuthal axis ($|\cos \Phi| > 0{\cdot}5$).

Table 3. Values of the mean swell characteristics measured at great depths on SAR images (SAR) and estimated by the Météofrance wave prediction model (MODEL), along with values of wind velocities W, measured on the shore, and W_c, as given by equation (13) and which represents the maximum value of the wind velocity for which the present method for estimating swell wave height is, theoretically, valid. Swell directions are referred to the west-east axis.

	Swell characteristics									
	Direction		Period(s)		Wave length (m)		Wave height (m)		Wind velocity ($m s^{-1}$)	
Date	SAR	MODEL	SAR	MODEL	SAR	MODEL	SAR	MODEL	W	W_c
25.11.1992	−52·8	−74	13·6	12·1	289	259	0·47	0·34	7	5·1
3.12.1992	−69·4	−74	15·4	17·4	368	491	0·39	0·99	8	6·9
30.12.1992	−52·4	n.a.	13·2	n.a.	273	n.a.	0·25	n.a.	9	4·8
7.1.1993	−37·0	−44	14·0	14·5	306	311	0·40	1·03	11	11·6
23.1.1993	−43·2	−44	12·5	12·1	243	298	0·15	0·31	11	7·5
26.1.1993	−48·5	−44	13·0	12·1	265	234	0·25	0·33	7	7·1

n.a. = not available.

observations and model results, as can be seen, for example, on figure 9, as compared to the SAR observations of figure 6(*a*). In particular, the zones of convergence-divergence of swell rays are nearly the same, and the spatial variations of H, deduced from imagery, are found consistent with these inhomogeneities: H decreases in regions of divergence and increases in regions of convergence.

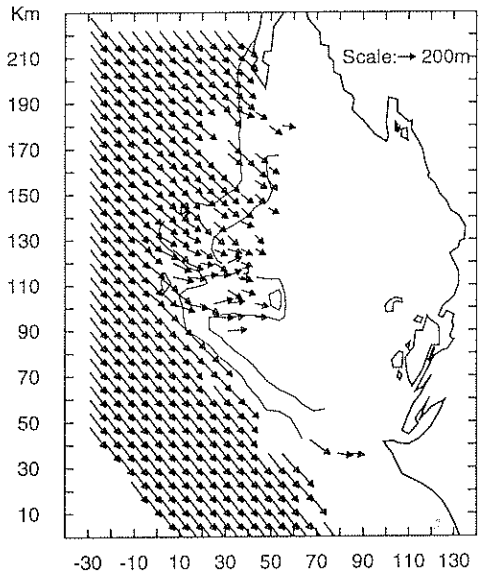

Figure 9. Modelling of swell wave lengths and directions by the ray method in the same conditions as in figure 6(*a*). The input wave field has the deep water characteristics given in table 2 (SAR). Spatial sampling is 6 km.

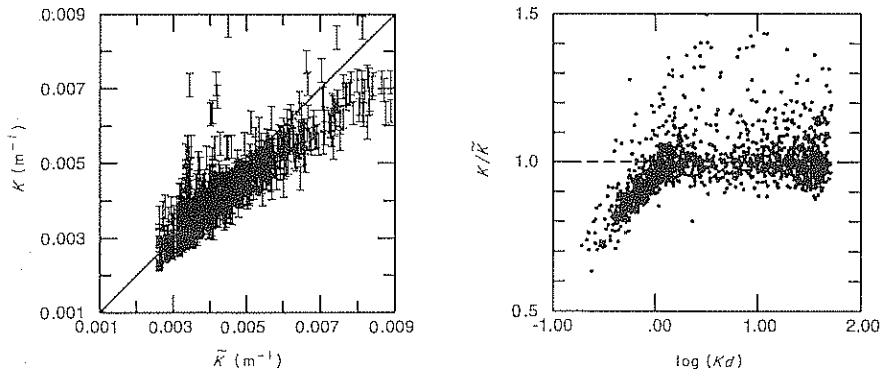

Figure 10. Comparison between radar estimates K and model estimates $\tilde{K}$ of swell wave number (*a*) K versus $\tilde{K}$, (*b*) $K/\tilde{K}$ versus the decimal logarithm of the non-dimensional number Kd (where d is the water depth).

However, systematic differences were observed on wave length measurements in shallow water. Figure 10 shows the results of comparison between SAR estimates K of the swell wave number and the theoretical values $\tilde{K}$ obtained from the equation, stating, under stationary conditions (no time-derivative for **K**), the conservation of the apparent frequency of a wave train (Phillips 1977). Without currents, and by the use of the linear surface wave dispersion relationship, we have:

$$K_0 = \tilde{K} \tanh \tilde{K} d \tag{15}$$

in which, here, the known parameters are the depth d (water depth of charts plus the sea level) and the mean wave number of the incident swell, K_0 (table 3). The results are presented in two diagrams. Figure 10(*a*) is a plot of K versus $\tilde{K}$, and figure 10(*b*), in normalized coordinates, is a plot of $K/\tilde{K}$ estimates versus the decimal logarithm of Kd. Clearly, SAR-derived estimates of the swell wave number are smaller than model predictions $\tilde{K}$, and this happens for Kd lower than unity. This means that SAR wave length estimates are over-estimated and/or that intense currents contribute to the lengthening, in general, of the swell wave lengths.

Let us consider the first hypothesis. Wave number distortions are essentially due to the influence of the fall-off function characterizing the smearing in azimuth of SAR images. This influence consists in a shift towards the range wave number axis of the position of the peak of the wave spectrum, in such a manner that waves appear longer and more range-travelling than they actually are (Shuchman *et al.* 1983). For the model of swell spectrum described by (7) and for a fall-off function in $\exp(-k_x^2/2\sigma_c^2)$ with $\sigma_c = 2\pi/\lambda_c$ (Monaldo and Lyzenga 1986), it is easy to show that the image spectrum of a swell of true wave number K_{true} and direction Φ_{true} peaks at a wave number $K = nK_{\text{true}}$ where n, the wave number distortion rate, is given by:

$$n = \left(\sin^2 \Phi_{\text{true}} + \frac{\cos^2 \Phi_{\text{true}}}{(1 + \sigma^2/\sigma_c^2)^2} \right)^{1/2} \tag{16}$$

To have an estimate of n, we considered the following typical values: $\sigma = 0{\cdot}005$ rd m^{-1} (as measured on predicted wave spectra in deep water); $\sigma_c = 0{\cdot}012$ rd m^{-1}

(equations (12)–(14), wind velocity of 9 m s^{-1} and fetch of 50 km). For Φ_{true} varying from 30° to 70° (or 210° to 250°), as suggested by present ERS-1 images, n varies from 0·89 to 0·98. Although evaluated coarsely, these values could explain part of the observations of figure 10. However, our data do not seem to depend on swell direction, and, in particular, the ratios $K/\tilde{K}$ cannot be scaled according to (16). For example, figure 11 is a plot of $K/\tilde{K}$ estimates versus the logarithm of Kd for $Kd<0{\cdot}5$ for the swell travelling close to the azimuth direction of figure 6(*a*) and for the swell travelling close to the range direction of figure 6(*c*). For these two well distinct situations, with regard to swell directions of propagation, the values of $K/\tilde{K}$ in shallow water and their variations with Kd are essentially the same. We conclude that the contribution of the SAR imaging mechanisms, if it exists, is not sufficient to explain the wave number differences of figure 10.

In order to discuss on current effects (second hypothesis), we mapped the component u of the current along the swell direction of propagation, which could explain the observed discrepancies in wave length measurements. In presence of currents, the conservation of the apparent frequency of a wave train gives (Phillips 1977):

$$\sqrt{gK\tanh Kd}+Ku=\sqrt{gK_0} \tag{17}$$

from which we have:

$$u=\frac{1}{K}(\sqrt{gK_0}-\sqrt{gK\tanh Kd}) \tag{18}$$

These equations rely on the assumption that the current velocity is negligible off-shore (great depths) and consider that, there, SAR estimates of the wave number, K_0, represent the true values of this parameter. Figure 12 shows the values of u for the case of figure 6(*a*). Significant velocities are met only over the bottom slope between iso-depths 10 m and 50 m, which is related to the fact that the above

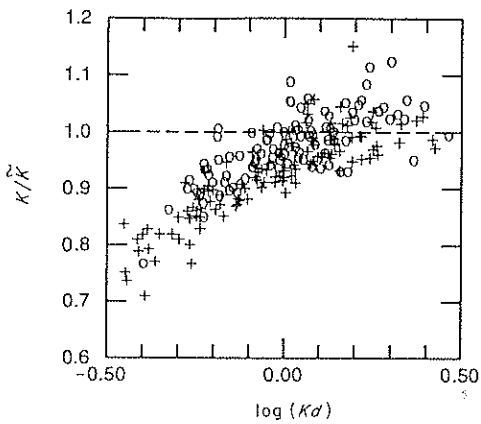

Figure 11. Same as in figure 10(*b*) for the swell observations of figure 6(*a*) (crosses) and figure 6(*c*) (circles) in intermediate water depths and in regions of low refraction (north of the ordinate 130 km on figure 5).

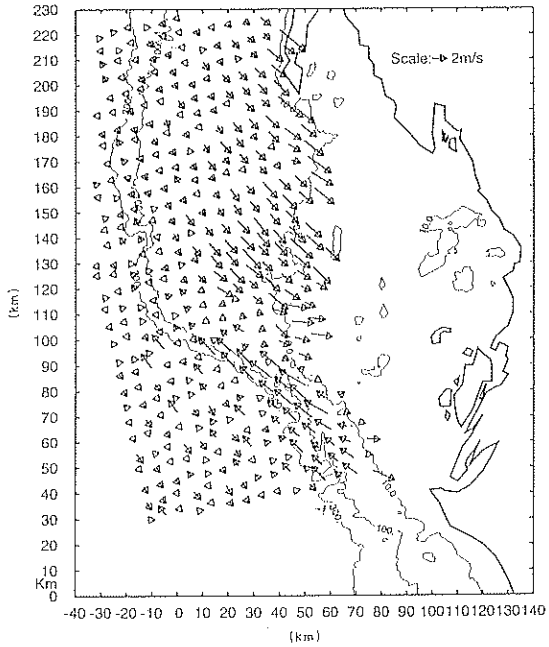

Figure 12. Map of the component of the current along swell direction which could explain the discrepancies between radar and model estimates of K for the case of figure 6(*a*).

discrepancies observed on wave length estimates occurred for $Kd < 1$. Velocities as high as 8 knots are found. Rather similar results have been obtained for all the other dates. The values of u have been compared with the velocity of the tidal current in front of Cap Blanc, u_T, deduced from the data edited by the French 'Service Hydrographique et Océanographique de la Marine' (1965). The results are listed in table 4. It appears that, despite the variety of tidal coefficients (in the range 51 to 91)

Table 4. Characteristics of the tidal current in front of Cap Blanc (approximate coordinates (40 km, 200 km) in the reference frame of figure 5), and comparison of its modulus, u_T, to the current velocity component along the wave propagation direction, u, calculated by equation (18).

			Tidal current		
Date	Phase	Tidal coefficient	u_T (knots)	Direction	u (knots)
25.11.1992	HT − 40′	91	0·7	SE	6
3.12.1992	LT + 10′	57	0·5	SE	6
30.12.1992	LT + 3 h	51	0·7	SE	4
7.1.1993	HT + 1 h 30′	70	0·3	SE	4
23.1.1993	HT − 55′	76	0·6	SE	n.a.
26.1.1993	HT − 1 h 50′	72	0·8	SE	n.a.

n.a. = not available

and tidal phases (from low tide +10 min to high tide +1h30) corresponding to our set of images, u_T values are of the same order, which is in agreement with the fact that differences in u measurements for the dates considered are small. It should be noted that this latter observation is closely related to the relatively low scatter of data points about the tail that can be seen on figure 10(*b*) for Kd lower than unity: the form of the tail is practically independent of the date of acquisition. But one important result is that u is much higher than u_T. We may conclude that the discrepancies between SAR-derived and theoretical values of swell wave number would persist if a model tidal current field was available, at least by using (18) as it has already been done by, e.g. Barnett *et al.* (1989) and Liu *et al.* (1994) in SAR studies on wave-current interactions (no topographic effect was considered). In fact, it has been demonstrated recently that wave transformations, in particular wave length variations, are fundamentally influenced by the propagation of the tidal wave, which leads to unsteady current and depth variations (Tolman 1990). Thus, a complete modelling of the kinematical transformations of our swell systems propagating over a varying field of current (itself given by modelling) and depth would be necessary to analyse the present results. Also, other currents than tidal currents (in particular, those currents controlled by the geostrophic northern Canary Current, Sevrin-Reyssac 1993) might be taken into account.

5. Conclusions

We presented a method to derive the main parameters of swell waves from SAR data. This method is based, for wave height estimates, on simplifications of the general theory of SAR wave imaging ('quasi-linear approximation'). This latter method has been used to assess the pertinence of these simplifications in the case of swells. The influence of wind waves on SAR wave height determination has been analysed, and it has been stressed that, for satellite SARs like on ERS-1, conditions of low to moderate wind conditions were required, for the method to hold. The method has been applied to a set of ERS-1 images of the shelf sea off Mauritanian coasts and presenting swell events. Swell maps obtained by SAR gives a detailed description of the phenomenon, and the reasonable agreement found between SAR- and model-derived estimates of the wave parameters allows us to be confident with SAR measurements. The analysis of swell wave length measurements in intermediate and shallow water have revealed discrepancies with regard to the theoretical values obtained without currents. These discrepancies have been interpreted as the signature of currents in a complex way which would necessitate the disposal of both a spatial and temporal description of the current field. The transformations of the swell in the coastal zone observed in this study are of scientific interest, and we may conclude that scientific applications, for which the spatial coverage of SAR images is of fundamental interest, can be henceforth envisaged on the basis of SAR-derived swell measurements.

Acknowledgments

This work was supported by the Centre National d'Etudes Spatiales under grant 91/CNES/0337. ERS-1 SAR data were supplied by ESA (ERS-1 scientific investigations, proposal F-16).

References

ALPERS, W., 1983, Monte Carlo simulations for studying the relationship between ocean wave and synthetic aperture radar image spectra. *Journal of Geophysical Research*, **88**, 1745–1759.

ALPERS, W. R., ROSS, D. B., and RUFENACH, C. L., 1981, On the detectability of ocean surface waves by real and synthetic radar. *Journal of Geophysical Research*, **86**, 6481–6498.

APRIL, G. V., and HARVEY, E. R., 1991, Speckle statistics in four-look synthetic aperture radar imagery. *Optical Engineering*, **30**, 375–381.

BEAL, R. C., TILLEY, D. G., and MONALDO, F. M., 1983, Large- and small-scale spatial evolution of digitally processed spectra from the Seasat synthetic aperture radar. *Journal of Geophysical Research*, **88**, 1761–1778.

BEAL, R. C., GERLING, T. W., MONALDO, F. M., and TILLEY, D. G., 1991, Measuring ocean waves from space. *International Journal of Remote Sensing*, **12**, 1713–1722.

BARNETT, T. P., KELLEY, F., and HOLT, B., 1989, Estimation of the two-dimensional ocean current shear field with a synthetic aperture radar. *Journal of Geophysical Research*, **94**, 16087–16095.

BRÜNING, C., SCHMIDT, R., and ALPERS, W., 1994, Estimation of the ocean wave-radar modulation transfer function from synthetic aperture radar imagery. *Journal of Geophysical Research*, **99**, 9803–9815.

CARTER, R. W. G., 1988, *Coastal Environments* (London: Academic Press).

CUQ, F., 1992, Detecting wave diffraction around Chassiron Point (Ile d'Oléron, Charente Maritime, France) using a SPOT-1 image. *Photo-Interpretation*, **7**, 63–68.

FORGET, P., 1994, Monitoring of swell by ERS-1 SAR imagery. *Proceedings of the Second ERS-1 Workshop held in Brest, France, on 15–17 March 1994* (in press).

GODA, Y., 1985, *Random Seas and Design of Maritime Structures* (Tokyo: University of Tokyo Press).

GOLDFINGER, A. D., 1982, Estimation of spectra from speckled images. *I.E.E.E. Transactions on Aerospace and Electronic Systems*, **18**, 675–681.

GRISWOLD, G. M., 1963, Numerical calculation of wave refraction. *Journal of Geophysical Research*, **68**, 1715–1723.

HASSELMANN, K., and HASSELMANN, S., 1991, On the nonlinear mapping of an ocean wave spectrum into a synthetic aperture radar image spectrum and its inversion. *Journal of Geophysical Research*, **96**, 10713–10729.

HASSELMANN, K., ROSS, D. B., MULLER, P., and SELL, W., 1976, A parametric wave prediction model. *Journal of Physical Oceanography*, **6**, 200–228.

HASSELMANN, K., RANEY, R. K., PLANT, W. J., ALPERS, W., SCHUCHMAN, R. A., LYZENGA, D. R., RUFENACH, C. L., and TUCKER, M. J., 1985, Theory of synthetic aperture radar ocean imaging: a MARSEN view. *Journal of Geophysical Research*, **90**, 4659–4686.

JOHNSEN, H., HOGDA, K. A., GUNERIUSSEN, T., and PEDERSEN, J. P., 1991, Azimuth smearing in synthetic aperture radar ocean image spectra from the Norwegian Continental Shelf Experiment of 1988. *Journal of Geophysical Research*, **96**, 10443–10452.

KASILIGAM, D. P., and SHEMDIN, O., 1990, Models for synthetic aperture radar imaging of the ocean: A comparison. *Journal of Geophysical Research*, **95**, 16263–16276.

KROGSTAD, H. E., SAMSET, O., and VACHON, P. W., 1994, Generalizations of the non-linear ocean-SAR transform and a simplified SAR inversion algorithm. *Atmosphere-Ocean*, **32**, 61–82.

LEE, J.-S., 1981, Speckle analysis and smoothing of synthetic aperture radar images. *Computer Graphics and Image Processing*, **17**, 24–32.

LIU, A. K., PENG, C. Y., and SCHUMACHER, J. D., 1994, Wave-current interaction study in the Gulf of Alaska for detection of eddies by synthetic aperture radar. *Journal of Geophysical Research*, **99**, 10075–10085.

LYZENGA, D. R., 1986, Numerical simulation of synthetic aperture radar image spectra of ocean waves. *I.E.E.E. Transactions on Geoscience and Remote Sensing*, **24**, 863–872.

MACKLIN, J. T., and CORDEY, R. A., 1991, Seasat SAR observations of ocean waves. *International Journal of Remote Sensing*, **12**, 1723–1740.

MATHIESEN, M., 1987, Wave refraction by a current whirl. *Journal of Geophysical Research*, **92**, 3905–3912.

METTLACH, T., WANG, D., and WITTMANN, P., 1994, Analysis and prediction of ocean swell using instrumented buoys. *Journal of Atmospheric and Oceanic Technology*, **11**, 506–524.

MONALDO, F. M., and LYZENGA, D. R., 1986, On the estimation of wave slope- and height-variance spectra from SAR imagery. *I.E.E.E. Transactions on Geoscience and Remote Sensing*, **24**, 543–551.

MONALDO, F. M., GERLING, T. G., and TILLEY, D. G., 1993, Comparison of SIR-B SAR wave image spectra with wave model predictions: implications on the SAR modulation transfer function. *I.E.E.E. Transactions on Geoscience and Remote Sensing*, **31**, 1199–1209.

OCAMPO-TORRES, F. J., and ROBINSON, I. S., 1989, Wind-directional effects on the hydrodynamic modulation of microwave radar images of ocean waves. *International Journal of Remote Sensing*, **10**, 1339–1355.

OLIVIER, P., and VIDAL MADJAR, D., 1994, Empirical estimation of the ERS-1 SAR radiometric resolution. *International Journal of Remote Sensing*, **15**, 1109–1114.

PHILLIPS, O. M., 1977, *The Dynamics of the Upper Ocean* (Cambridge: Cambridge University Press).

PIERSON, W. J., and MOSKOWITZ, L., 1964, A proposed spectral form for fully developed wind seas based on the similarity theory of S. A. Kitaigorodskii. *Journal of Geophysical Research*, **69**, 5181–5190.

RUFENACH, C. L., SHUCHMAN, R. A., MALINAS, N. P., and JOHANNESSEN, J. A., 1991, Ocean wave spectral distortion in airborne synthetic aperture radar imagery during the Norwegian Continental Shelf Experiment of 1988. *Journal of Geophysical Research*, **92**, 10453–10466.

SEVRIN-REYSSAC, J., 1993, Hydrology and underwater climate of the Banc d'Arguin, Mauritania: a review. *Hydrobiologia*, **258**, 1–8.

SHEMDIN, O. H., HSIAO, S. V., CARLSON, H. E., HASSELMANN, K., AND SCHULZE, K., 1980, Mechanisms of wave transformation in finite-depth water. *Journal of Geophysical Research*, **85**, 5012–5018.

SCHUCHMAN, R. A., LYDEN, J. D., and LYZENGA, D. R., 1983, Estimates of ocean wavelength and direction from X- and L-band synthetic aperture radar data collected during the Marineland experiment. *I.E.E.E. Journal of Oceanic Engineering*, **8**, 90–96.

TILLEY, D. G., and BEAL, R. C., 1994, ERS-1 and Almaz estimates of directional ocean wave spectra conditioned by simultaneous aircraft SAR and buoys measurements. *Atmoshpere-Ocean*, **32**, 113–142.

TOLMAN, H L., 1990, The influence of unsteady depths and tidal currents on wind-wave propagation in shelf seas. *Journal of Physical Oceanography*, **20**, 1166–1174.

TUCKER, M. J., 1985, The imaging of waves by satellite synthetic aperture radar: the effects of surface motion. *International Journal of Remote Sensing*, **6**, 1059–1074.

WOLFF, W. J., VAN DER LAND, J., NIENHUIS, P. H., and DE WILDE, P. A. W. J., (editors), 1993, *Ecological Studies in the Coastal Waters of Mauritania* (Dordrecht: Kluwer Academic Publishers).